ISA Transactions 114 (2021) 347–358

Contents lists available at ScienceDirect

ISA Transactions

journal homepage: www.elsevier.com/locate/isatrans

Practice article

Robust predictive visual servoing control for an inertially stabilized platform with uncertain kinematics

Xiangyang Liu [a], Jianliang Mao [b,c], Jun Yang [d], Shihua Li [a,*], Kaifeng Yang [c]

[a] School of Automation, Southeast University, Key Laboratory of Measurement and Control of Complex Systems of Engineering, Ministry of Education, Nanjing 210096, PR China
[b] College of Automation Engineering, Shanghai University of Electric Power, Shanghai 200090, PR China
[c] R & D Institute of ESTUN AUTOMATION CO., LTD, Nanjing 211106, PR China
[d] Department of Aeronautical and Automotive Engineering, Loughborough University, Loughborough LE11 3TU, UK

ARTICLE INFO

Article history:
Received 19 February 2020
Received in revised form 14 December 2020
Accepted 21 December 2020
Available online 4 January 2021

Keywords:
Model predictive control
Uncertain kinematics
Image-based visual servoing
Disturbance observer
Inertially stabilized platform

ABSTRACT

In this paper, a disturbance observer (DOB) based predictive control approach is developed for the image-based visual servoing of an inertially stabilized platform (ISP). As the limitation in degrees of freedom of a two-axes ISP, it is hard to estimate the variable feature depth of the target at each control cycle when using an uncalibrated camera, which brings the challenge in the design of the visual servoing controller. To this end, a depth-independent kinematic matrix that only involves nominal parameters is obtained by employing the partitioned scheme in the system modeling. The uncertain kinematics arising from the unknown feature depth, angular velocity tracking errors, and uncalibrated intrinsic parameters is considered as the lumped uncertainty. A discrete-time DOB is then constructed to estimate the lumped uncertainty in real time. Instead of taking an integral action to eliminate tracking errors induced by the uncertain kinematics, the disturbance estimation is actively incorporated into the receding optimization process of the predictive controller. The stability of the closed-loop system is fully analyzed. Experiments on tracking a moving target are performed to validate promising qualities of the proposed approach.

1. Introduction

Inertially stabilized platforms have been extensively utilized for a wide range of moving carriers, such as satellites, aircrafts, submarines, etc [1–3], due to the superior isolation ability against carrier motion and vibration. The basic task of an ISP is to make the light of sight (LOS) of the optical sensor installed on a mobile vehicle precisely track a moving target or keep steady in inertial space [4,5]. For the target tracking, the control structure usually includes the outer tracking loop and the inner stabilized loop [6]. The outer loop is to lock the target via the visual signal and produces the desired inertial angular velocity as the inner-loop reference, furthermore, the inner stabilized loop adjusts the camera to the given inertial angular velocity by using a gyroscope. To date, most of literatures have focused on improving the control performances of the low-level stabilized loop and obtained many satisfactory results [7–9]. Recently, in order to obtain a higher control performance of the inner loop, a more elaborate system model considering the asymmetric mass distribution has been established in [10], then the DOB based continuous-time TSMC approach has been proposed for the disturbance suppression. In contrast, only a few results on the high-level visual servoing of an ISP can be retrieved.

In reality, due to the strong ability of the environmental perception, the visual servoing control has been widely applied in many fields over the past decade, such as wheeled mobile robots [11,12], multi-joint manipulators [13,14], and unmanned vehicles [15,16]. The underlying idea in these applications is to exploit the visual information captured from the camera for the motion control of a platform [17]. Generally, vision-based control approaches can usually be classified as the position-based visual servoing (PBVS) and the image-based visual servoing (IBVS) [18]. A comprehensive introduction to both categories can be found in [19]. The PBVS generally involves the complicated problem of the 3-dimensional (3D) reconstruction, while the IBVS directly map an image feature error function to adjust the motion of the equipment. Consequently, the IBVS method exhibits more concise and efficient qualities especially when 3D coordinates in the world frame is difficult to establish, which thereby is more practical for the visual servoing of an ISP [20].

Although the classical IBVS scheme is robust to the modeling and camera calibration uncertainties, applying IBVS to an ISP system still suffers from two major challenges. One issue

* Corresponding author.
E-mail address: lsh@seu.edu.cn (S. Li).

https://doi.org/10.1016/j.isatra.2020.12.039
0019-0578/

is the inevitable angular velocity tracking errors from the inner loop, which are largely affected by cross-couplings and the mass imbalance when the carrier motion exists [21]. Therefore, the inner-loop tracking errors will affect as the time-varying disturbances imposing on the input channel of the high-level visual servoing loop. The other challenge stems from the target motion with the unknown variable feature depth. It is explicit that the implementation of IBVS is generally based on an interaction matrix that relies on the depth information of each feature point. However, in practice, the exact real-time knowledge of the feature depth is hard to access directly. A straightforward method is to take a fixed priori value for the depth and then use the resulting constant interaction matrix to construct the feedback control law [22]. Such simplification may fail in the presence of time-varying feature depth. In addition, a majority of efforts have been devoted to real-time estimations of unknown parameters involving the depth information by virtue of the designed control laws [23]. Nevertheless, the relevant control schemes are raised for approaching a geostationary target object, not yet suitable for the purpose of the moving target tracking. As such, alleviating the adverse impacts caused by uncertain kinematics in the presence of both carrier and target motions becomes a primary concern in the IBVS of ISPs.

Since the computer vision system transfers the image feature information at discrete instants, the visual servoing loop is essentially a sampled system with a relatively low frequency [24]. For discrete-time systems [25,26], the model predictive control (MPC) approach, by applying the receding horizon control to perform the on-line optimization, holds the superior properties with intuitive concept and flexible tuning. As the system model plays a crucial role in the output prediction process, the aforementioned kinematic uncertainty usually brings a large performance degradation of the MPC approach. For disturbance and uncertainty rejection, a simple way is to embed an integral action in the MPC designs (see [27] for details). On this occasion, however, the offset-free property is obtained at the expense of several performance sacrifices such as the large overshoot. As an alternative approach for attenuating model uncertainties and external disturbances in control systems, the disturbance estimation-based control has received widespread attentions in recent years [28,29]. A DOB based continuous MPC method has been designed for the converter, without considering the control input weighting in the stability analysis [30].

In this paper, we concentrate on developing a DOB-based MPC approach for the visual servoing of an ISP system. A depth-independent kinematic matrix that only involves nominal parameters is firstly obtained by employing the partitioned approach in the system modeling. The uncertain kinematics arising from the unknown feature depth, inner-loop angular rate tracking errors, and uncalibrated intrinsic parameters is considered as the lumped uncertainty. The discrete-time DOB is then constructed to estimate the lumped uncertainty in real time. Instead of taking an integral action to eliminate the tracking error induced by the uncertain kinematics, a disturbance estimation is actively incorporated into the receding optimization process of the model predictive controller such that the output prediction accuracy is greatly enhanced. It is shown that the target tracking error asymptotically converges to a bounded region even in the presence of time-varying uncertainties. Finally, to reveal the effective advantages of the proposed method, experiments including the parameters selection and performance comparisons are conducted. The main contributions of this paper are concluded as follows:

1. *By dealing with the uncertain kinematics arising from the unknown variable feature depth of the target and inner-loop tracking errors, a DOB based predictive controller is developed for the visual servoing of an ISP with an uncalibrated camera, which obtains an easy design property and the high efficiency in tracking a moving target.*
2. *The control input weighting in the modified cost function is designed with more tuning degrees of freedom than that in [30], thereby achieving a better optimization performance in the presence of time-varying uncertainties.*
3. *The stability of the closed-loop system is fully analyzed with the combination of the disturbance observer and the predictive controller considering weighting matrices on tracking errors as well as control inputs.*

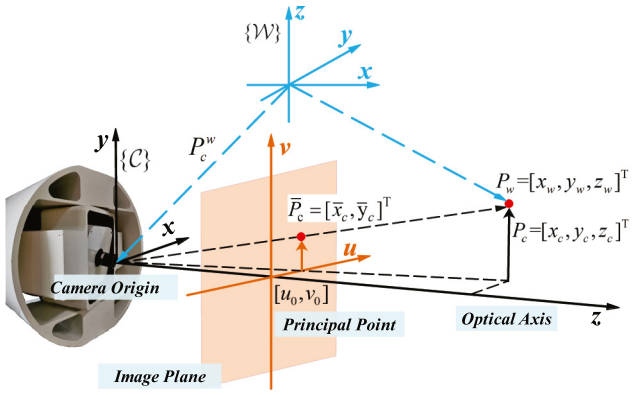

Fig. 1. Coordinate system of the two-axes ISP.

The remainder of this paper is organized as follows. In Section 2, the kinematics modeling of the IBVS of an ISP system is illustrated in detail. In Section 3, the proposed DOB-based MPC approach associated with the stability analysis is introduced. The experimental verification is performed in Section 4. The conclusions are drawn in Section 5.

2. Problem formulation

2.1. Useful properties

The following properties are helpful for subsequent derivations [19]:

(i) For any matrix $R \in SO(3)$, since the R is orthogonal, $RR^{\mathrm{T}} = I$, where $SO(3)$ is the 3D rotation group.
(ii) For any vectors $a, b \in \mathbb{R}^3$, $\mathcal{S}(a)b = a \times b$ and $\mathcal{S}^{\mathrm{T}}(a) = -\mathcal{S}(a)$, where $\mathcal{S}(a)$ denotes a skew symmetric matrix based on the vector a.
(iii) For any matrix $R \in SO(3)$ and vectors $a, b \in \mathbb{R}^3$, $R(a \times b) = (Ra) \times (Rb)$.

2.2. Configuration

The two-axes ISP contains the pitch and yaw gimbal frames, directly driven by torque motors. The camera requiring isolation from the carrier disturbance is placed on the inner pitch gimbal. As mentioned, the cascaded control structure is commonly taken for the ISP system. Generally, the bandwidth of the inner stabilized loop is much higher than that of the outer tracking loop, so that the commanded inertial angular rates of the camera are almost followed by the inner stabilized loop. As such, in order to design a visual servoing controller, the dynamic model between the input signal (i.e., the desired inertial angular velocity of the camera) and the output signal (i.e., the pixel coordinate of the target in the image plane) is expected to be developed.

2.3. Visual servoing kinematics

To describe the dynamic model of the image-based visual servoing system of an ISP, two coordinate frames are introduced: the camera frame $\{\mathcal{C}\}$ and the world frame $\{\mathcal{W}\}$. In Fig. 1, coordinates of the moving target in 3D space relative to the frames $\{\mathcal{C}\}$ and $\{\mathcal{W}\}$ are denoted as $P_c = [x_c, y_c, z_c]^{\mathrm{T}}$ and $P_w = [x_w, y_w, z_w]^{\mathrm{T}}$, respectively, the coordinate of the frame $\{\mathcal{C}\}$ with respect to the frame $\{\mathcal{W}\}$ is defined by $P_c^w = [x_c^w, y_c^w, z_c^w]^{\mathrm{T}}$, and the rotation matrix from the frame $\{\mathcal{C}\}$ to the frame $\{\mathcal{W}\}$ is given as $R_c^w \in \mathbb{R}^{3\times 3}$. Furthermore, letting $\Omega_c = [\omega_x, \omega_y, \omega_z]^{\mathrm{T}}$ and $V_c = [v_x, v_y, v_z]^{\mathrm{T}}$ denote the inertial angular velocity and line velocity of the camera both expressed in the frame $\{\mathcal{C}\}$, respectively, and Ω_w denotes the angular velocity of the moving camera expressed in the frame $\{\mathcal{W}\}$. Then, the following kinematics can be presented [19]:

$$\begin{aligned} &\dot{R}_c^w = \mathcal{S}(\Omega_w)R_c^w,\ \Omega_w = R_c^w\Omega_c, \\ &\dot{P_c^w} = R_c^w V_c,\ P_c = (R_c^w)^{\mathrm{T}}(P_w - P_c^w). \end{aligned} \tag{1}$$

The motion of the target can be described by differentiating P_c as

$$\dot{P}_c = (\dot{R}_c^w)^{\mathrm{T}}(P_w - P_c^w) + (R_c^w)^{\mathrm{T}}(\dot{P}_w - \dot{P}_c^w). \tag{2}$$

Under Properties (i)–(iii), by substituting (1) into (2), one obtains

$$\begin{aligned} \dot{P}_c &= (R_c^w)^{\mathrm{T}}[S^{\mathrm{T}}(\Omega_w)(P_w - P_c^w)] + (R_c^w)^{\mathrm{T}}\dot{P}_w - V_c \\ &= -(R_c^w)^{\mathrm{T}}[\Omega_w \times (P_w - P_c^w)] + (R_c^w)^{\mathrm{T}}\dot{P}_w - V_c \\ &= -\Omega_c \times P_c + (R_c^w)^{\mathrm{T}}\dot{P}_w - V_c. \end{aligned} \tag{3}$$

Suppose that the projection of P_c in the image plane is defined by $\bar{P}_c = [\bar{x}_c, \bar{y}_c]^{\mathrm{T}}$ and the pixel coordinates of $\bar{P}_c$ is given by $S = [u, v]^{\mathrm{T}}$. Moreover, assume that the image formation process can be expressed by the pinhole lens model. By means of the perspective projection theory [19], the image feature vector can be calculated as

$$\begin{bmatrix} S \\ 1 \end{bmatrix} = \begin{bmatrix} k_x & 0 & u_0 \\ 0 & k_y & v_0 \\ 0 & 0 & 1 \end{bmatrix} \begin{bmatrix} \bar{P}_c \\ 1 \end{bmatrix}, \begin{bmatrix} \bar{P}_c \\ 1 \end{bmatrix} = \frac{1}{z_c} \begin{bmatrix} \lambda & 0 & 0 \\ 0 & \lambda & 0 \\ 0 & 0 & 1 \end{bmatrix} P_c \tag{4}$$

where k_x and k_y are the scale factors between pixel and meter in the x and y directions, respectively, u_0 and v_0 are the principal point coordinates of the image in pixels, and λ is the focal length of the camera, which are also called the intrinsic parameters.

Generally, the relationship between the image feature velocity and the inertial angular velocity of the camera is supposed to be established for the IBVS control system [19]. To this end, by differentiating (4), we have

$$\dot{u} = k_x\lambda\frac{\dot{x}_c z_c - x_c\dot{z}_c}{z_c^2},\ \dot{v} = k_y\lambda\frac{\dot{y}_c z_c - y_c\dot{z}_c}{z_c^2}. \tag{5}$$

Substituting (3) into (5), it yields

$$\dot{S} = L_\omega(S)\Omega_c + L_v(S, z_c)[V_c - (R_c^w)^{\mathrm{T}}\dot{P}_w] \tag{6}$$

where $[L_v, L_\omega] \in \mathbb{R}^{2\times 6}$ is known as the image interaction matrix, expressed by

$$L_v = \begin{bmatrix} -\frac{\lambda k_x}{z_c} & 0 & \frac{u-u_0}{z_c} \\ 0 & -\frac{\lambda k_y}{z_c} & \frac{v-v_0}{z_c} \end{bmatrix},$$

$$L_\omega = \begin{bmatrix} \frac{(u-u_0)(v-v_0)}{\lambda k_y} & -\frac{(\lambda k_x)^2+(u-u_0)^2}{\lambda k_x} & \frac{k_x(v-v_0)}{k_y} \\ \frac{(\lambda k_y)^2+(v-v_0)^2}{\lambda k_y} & -\frac{(u-u_0)(v-v_0)}{\lambda k_x} & -\frac{k_y(u-u_0)}{k_x} \end{bmatrix}.$$

Remark 1. In the existing research works of IBVS systems [13,15,23], the target is assumed to be geostationary, i.e., $\dot{P}_w = 0$. On the contrary, the one considered in this paper may be moving, which yields the non-vanishing term $(R_c^w)^{\mathrm{T}}\dot{P}_w$. Namely, the target motion imposes the disturbance on the input channel of the ISP visual servoing system.

Remark 2. In practice, the exact knowledge of the time-varying feature depth z_c is hard to acquire in real time, which brings a problem in the design of the visual servoing controller. Therefore, the partitioned method introduced in [19] is exploited to decompose system (6) to obtain a depth-independent matrix L_ω.

2.4. Problem formulation

Assume that nominal values of camera intrinsic parameters are known and denoted as k_x^*, k_y^*, and λ^*, respectively. Considering that only two degrees of freedom, i.e., angular velocities ω_x and ω_y are available for the attitude adjustment of the camera in the configuration, we rearrange system (6) as

$$\dot{S} = L_u^*(S)U_s + D(t) \tag{7}$$

where $U_s = [\omega_x^*, \omega_y^*]^{\mathrm{T}}$ is taken as the control input, ω_x^* as well as ω_y^* are reference inertially angular velocities for the inner stabilized loop, $L_u^*(S)$ is the matrix with nominal values of the camera intrinsic parameters, expressed by

$$L_u^*(S) = \begin{bmatrix} \frac{(u-u_0)(v-v_0)}{\lambda^* k_y^*} & -\frac{(\lambda^* k_x^*)^2+(u-u_0)^2}{\lambda^* k_x^*} \\ \frac{(\lambda^* k_y^*)^2+(v-v_0)^2}{\lambda^* k_y^*} & -\frac{(u-u_0)(v-v_0)}{\lambda^* k_x^*} \end{bmatrix},$$

and $D(t)$ is viewed as the lumped disturbance arising from the unknown feature depth z_c, the line velocity of the camera V_c, the line velocity of the moving target $\dot{P}_w$, the inner-loop angular velocity tracking errors, and the uncertainties of the camera intrinsic parameters, denoted by

$$D(t) = L_v(S, z_c)[V_c - (R_c^w)^{\mathrm{T}}\dot{P}_w] + L_\omega(S)\Omega_c - L_u^*(S)U_s.$$

The control objective is to ensure the output $S = [u, v]^{\mathrm{T}}$ to lock the desired image feature $S_d = [u_0, v_0]^{\mathrm{T}}$ in spite of the lumped disturbance $D(t)$. That is, the error of S and S_d converges to a bounded domain as small as possible.

3. DOB-based discrete-time MPC

To begin with, the zero-order holder is employed for the discretization of dynamic model (7). By introducing a virtual control vector $U = L_u^*(S)U_s$, the discrete-time state-space model is presented as

$$\begin{cases} S(k+1) = AS(k) + B_u U(k) + B_d D(k), \\ Y(k) = S(k) \end{cases} \tag{8}$$

where $A = I_{2\times 2}, B_u = B_d = \mathrm{diag}\{T_s, T_s\}$ in which T_s is the sampling period of the discrete-time system.

3.1. Formulation of output prediction

In order to derive the future output, denoting the control sequence $\mathcal{U}$, the disturbance sequence $\mathcal{D}$, and the output prediction sequence $\mathcal{Y}$ as

$$\begin{aligned} &\mathcal{U} = [U(k)^{\mathrm{T}}, U(k+1)^{\mathrm{T}}, \cdots, U(k+N_c-1)^{\mathrm{T}}]^{\mathrm{T}}, \\ &\mathcal{D} = [D(k)^{\mathrm{T}}, D(k+1)^{\mathrm{T}}, \cdots, D(k+N_c-1)^{\mathrm{T}}]^{\mathrm{T}}, \\ &\mathcal{Y} = [Y(k+1|k)^{\mathrm{T}}, Y(k+2|k)^{\mathrm{T}}, \cdots, Y(k+N_p|k)^{\mathrm{T}}]^{\mathrm{T}} \end{aligned}$$

where $\mathcal{U} \in \mathbb{R}^{2N_c}$, $\mathcal{D} \in \mathbb{R}^{2N_c}$, $\mathcal{Y} \in \mathbb{R}^{2N_p}$, N_c and N_p are called the control horizon and the prediction horizon (see [27] for details), respectively, satisfying $N_p \geq N_c$. Then the following assumption is essential for the derivation of the proposed control method.

Assumption 1 ([27]). The disturbances and control inputs remain unchanged outside the control horizon, i.e.,

$$\begin{aligned} &D(k+i) = D(k+N_c-1), \\ &U(k+i) = U(k+N_c-1), \quad i = N_c, \cdots, N_p-1. \end{aligned} \tag{9}$$

Under Assumption 1, the predicted output variables can be calculated based on discrete-time model (8) as

$$\begin{aligned} Y(k+i|k) &= A^i S(k) + \sum_{j=0}^{i-1} A^{i-j-1}[B_u U(k+j) + B_d D(k+j)],\ i \le N_c, \\ Y(k+i|k) &= A^i S(k) + \sum_{j=0}^{i-N_c} A^j [B_u U(k+N_c-1) + B_d D(k+N_c-1)] \\ &\quad + \sum_{j=0}^{N_c-2} A^{i-j-1}[B_u U(k+j) + B_d D(k+j)],\ i > N_c. \end{aligned} \tag{10}$$

For notational simplicity, sequence (10) can be rearranged as

$$\mathcal{Y} = FS(k) + \Phi_u \mathcal{U} + \Phi_d \mathcal{D} \tag{11}$$

where

$$F = \begin{bmatrix} A \\ A^2 \\ \vdots \\ A^{N_p} \end{bmatrix},$$

$$\Phi_u = \begin{bmatrix} B_u & O & \cdots & O \\ AB_u & B_u & \cdots & O \\ \vdots & \vdots & & \vdots \\ A^{N_c-1}B_u & A^{N_c-2}B_u & \cdots & B_u \\ A^{N_c}B_u & A^{N_c-1}B_u & \cdots & AB_u + B_u \\ \vdots & \vdots & & \vdots \\ A^{N_p-1}B_u & A^{N_p-2}B_u & \cdots & \sum_{m=0}^{N_p-N_c} A^m B_u \end{bmatrix},$$

$$\Phi_d = \begin{bmatrix} B_d & O & \cdots & O \\ AB_d & B_d & \cdots & O \\ \vdots & \vdots & & \vdots \\ A^{N_c-1}B_d & A^{N_c-2}B_d & \cdots & B_d \\ A^{N_c}B_d & A^{N_c-1}B_d & \cdots & AB_d + B_d \\ \vdots & \vdots & & \vdots \\ A^{N_p-1}B_d & A^{N_p-2}B_d & \cdots & \sum_{m=0}^{N_p-N_c} A^m B_d \end{bmatrix}.$$

Note that the sequence $\mathcal{Y}$ is directly affected by the disturbance sequence $\mathcal{D}$. Motivated by the design philosophy of the DOB based control method [29], the composition of the DOB based MPC is investigated to enhance the disturbance rejection performance in this paper. Define the $\hat{\mathcal{D}}$ as the estimation of the disturbance sequence $\mathcal{D}$ for the following derivations.

3.2. Cost function with disturbance compensation

In general, the objective of the MPC is to develop an optimized control sequence such that the error function between the reference sequence $\mathcal{S}$ and the predicted output sequence $\mathcal{Y}$ is minimized, where

$$\mathcal{S} = \overbrace{[I_{2\times 2}, \cdots, I_{2\times 2}]^{\mathrm{T}}}^{\mathcal{I}_{\mathcal{S}} \in \mathbb{R}^{2N_p \times 2}} S_d.$$

Toward this end, by actively incorporating the disturbance sequence estimate $\hat{\mathcal{D}}$, a novel generalized cost function is defined as

$$J = (\mathcal{S} - \hat{\mathcal{Y}})^{\mathrm{T}} \bar{\mathcal{Q}} (\mathcal{S} - \hat{\mathcal{Y}}) + (\mathcal{U} - \hat{\mathcal{U}})^{\mathrm{T}} \bar{\mathcal{R}} (\mathcal{U} - \hat{\mathcal{U}}) \tag{12}$$

where $\bar{\mathcal{Q}}$ is the weighting on the predictive tracking errors, $\bar{\mathcal{R}}$ is the weighting on the control inputs, $\hat{\mathcal{Y}}$ is the estimation based output prediction sequence, $\hat{\mathcal{U}}$ is the estimation based desired control sequence, and

$$\begin{aligned} \hat{\mathcal{Y}} &= FS(k) + \Phi_u \mathcal{U} + \Phi_d \hat{\mathcal{D}}, \\ \hat{\mathcal{U}} &= \Phi_u^{+}(\mathcal{S} - FS_d - \Phi_d \hat{\mathcal{D}}) \end{aligned}$$

in which $\Phi_u^{+} = (\Phi_u^{\mathrm{T}} \Phi_u)^{-1} \Phi_u^{\mathrm{T}}$ is the pseudoinverse of Φ_u.

Remark 3. The underlying idea of defined cost function (12) is based on the output regulation theory [31]. It can be derived from (11) that the desired steady-state values of $\mathcal{Y}$ and $\mathcal{U}$ are $\mathcal{Y}_{ss} = \mathcal{S}$ and $\mathcal{U}_{ss} = \Phi_u^{+}(\mathcal{S} - FS_d - \Phi_d \mathcal{D})$, respectively. To make the predicted output sequence $\mathcal{Y}$ and control sequence $\mathcal{U}$ are expected to be the desired steady-state values, the cost function is chosen as $J = (\mathcal{Y}_{ss} - \mathcal{Y})^{\mathrm{T}} \bar{\mathcal{Q}} (\mathcal{Y}_{ss} - \mathcal{Y}) + (\mathcal{U} - \mathcal{U}_{ss})^{\mathrm{T}} \bar{\mathcal{R}} (\mathcal{U} - \mathcal{U}_{ss})$. However, the predicted output $\mathcal{Y}$ and the desired steady-state control sequence $\mathcal{U}_{ss}$ here are dependent of the unobtainable disturbance sequence $\mathcal{D}$. The disturbance sequence estimate $\hat{\mathcal{D}}$ is thereby actively incorporated, resulting in cost function (12).

3.3. Receding horizon optimization

In order to find the optimal $\mathcal{U}$ that can minimize performance index (12), the cost function J is rearranged as

$$\begin{aligned} J = {} & [\Phi_u^{+}(\Phi_d \hat{\mathcal{D}} + FS_d - \mathcal{S})]^{\mathrm{T}} \bar{\mathcal{R}} \Phi_u^{+}(\Phi_d \hat{\mathcal{D}} + FS_d - \mathcal{S}) \\ & + [\mathcal{S} - FS(k) - \Phi_d \hat{\mathcal{D}}]^{\mathrm{T}} \bar{\mathcal{Q}} [\mathcal{S} - FS(k) - \Phi_d \hat{\mathcal{D}}] \\ & + \mathcal{U}^{\mathrm{T}} (\Phi_u^{\mathrm{T}} \bar{\mathcal{Q}} \Phi_u + \bar{\mathcal{R}}) \mathcal{U} - 2\mathcal{U}^{\mathrm{T}} \Phi_u^{\mathrm{T}} \bar{\mathcal{Q}} [\mathcal{S} - FS(k) - \Phi_d \hat{\mathcal{D}}] \\ & + 2\mathcal{U}^{\mathrm{T}} \bar{\mathcal{R}} \Phi_u^{+}(\Phi_d \hat{\mathcal{D}} + FS_d - \mathcal{S}) \end{aligned} \tag{13}$$

which is divided into dependent and independent terms with respect to $\mathcal{U}$. Taking the partial derivative of J with respect to $\mathcal{U}$ yields

$$\begin{aligned} \frac{\partial J}{\partial \mathcal{U}} = {} & 2\bar{\mathcal{R}} \Phi_u^{+}(\Phi_d \hat{\mathcal{D}} + FS_d - \mathcal{S}) + 2(\Phi_u^{\mathrm{T}} \bar{\mathcal{Q}} \Phi_u + \bar{\mathcal{R}}) \mathcal{U} \\ & - 2\Phi_u^{\mathrm{T}} \bar{\mathcal{Q}} [\mathcal{S} - FS(k) - \Phi_d \hat{\mathcal{D}}]. \end{aligned} \tag{14}$$

The necessary condition for minimizing J is attained by $\partial J / \partial \mathcal{U} = 0$, from which the optimized control sequence $\mathcal{U}^*$ is derived as

$$\begin{aligned} \mathcal{U}^* = {} & (\Phi_u^{\mathrm{T}} \bar{\mathcal{Q}} \Phi_u + \bar{\mathcal{R}})^{-1} [\Phi_u^{\mathrm{T}} \bar{\mathcal{Q}} (\mathcal{S} - FS(k) - \Phi_d \hat{\mathcal{D}}) \\ & - \bar{\mathcal{R}} \Phi_u^{+}(\Phi_d \hat{\mathcal{D}} + FS_d - \mathcal{S})]. \end{aligned} \tag{15}$$

According to the receding horizon control principle, only the first two elements of $\mathcal{U}^*$ is taken as the real-time control input, i.e.,

$$U^*(k) = \overbrace{[I_{2\times 2}, O_{2\times 2}, \cdots, O_{2\times 2}]}^{\mathcal{I}_{\mathcal{U}} \in \mathbb{R}^{2\times 2N_c}} \mathcal{U}^*. \tag{16}$$

Combining Eqs. (15) and (16), the optimized control law $U^*(k)$ can be rearranged as

$$\begin{aligned} U^*(k) = {} & \underbrace{\mathcal{I}_{\mathcal{U}} (\Phi_u^{\mathrm{T}} \bar{\mathcal{Q}} \Phi_u + \bar{\mathcal{R}})^{-1} [\Phi_u^{\mathrm{T}} \bar{\mathcal{Q}} \mathcal{I}_{\mathcal{S}} + \bar{\mathcal{R}} \Phi_u^{+}(\mathcal{I}_{\mathcal{S}} - F)]}_{K_s} S_d \\ & - \underbrace{\mathcal{I}_{\mathcal{U}} (\Phi_u^{\mathrm{T}} \bar{\mathcal{Q}} \Phi_u + \bar{\mathcal{R}})^{-1} \Phi_u^{\mathrm{T}} \bar{\mathcal{Q}} F}_{K_m} S(k) \\ & - \underbrace{\mathcal{I}_{\mathcal{U}} (\Phi_u^{\mathrm{T}} \bar{\mathcal{Q}} \Phi_u + \bar{\mathcal{R}})^{-1} (\Phi_u^{\mathrm{T}} \bar{\mathcal{Q}} \Phi_d + \bar{\mathcal{R}} \Phi_u^{+} \Phi_d)}_{K_d} \hat{\mathcal{D}}. \end{aligned} \tag{17}$$

Since it can be found that $B_u = B_d$ in (8) and $\Phi_u = \Phi_d$ in expression (11), the K_d simplifies to $\mathcal{I}_{\mathcal{U}}$ and then $K_d \hat{\mathcal{D}} = \hat{D}(k)$ in Eq. (17), in which $\hat{D}(k)$ is the estimation of the current disturbance $D(k)$. Therefore, one obtains

$$U^*(k) = K_s S_d - K_m S(k) - \hat{D}(k). \tag{18}$$

Consequently, the actual control signal can be calculated by

$$U_s = (L_u^*(S))^{-1}U^*(k). \tag{19}$$

3.4. DOB design

In this section, a discrete-time DOB is designed to estimate the lumped disturbance $D(k)$. First, define $D(k) = [d_1(k), d_2(k)]^{\mathrm{T}}$. The following mild assumption is then presented before the DOB design.

Assumption 2 ([28]). The variation of the disturbance $d_i(k)$ is always bounded by the positive constant ε_i, i.e.,

$$|\Delta d_i(k)| \le T_s \cdot \varepsilon_i, i = 1, 2 \tag{20}$$

where $\Delta d_i(k) = d_i(k) - d_i(k-1)$.

In general, the lumped disturbance as well as its difference usually contain states of the system. As known for the disturbance estimation and compensation approaches [29,32,33], it is not easy to prove the stability of the close-loop system with this general case of $\Delta d_i(k)$. In many practical projects, the system states are often stabilized by the basic feedback controller, and the uncertainty caused by system states is relatively weak, which will not affect the stability of the system. This is possibly the major reason for the prevalence of using the disturbance estimation and compensation based control method to restrain the inside uncertainty in the engineering application.

Motivated by [28], the discrete-time DOB is constructed to estimate the lumped disturbance $D(k)$ as

$$\begin{cases} Z(k+1) = Z(k) - K[B_u U(k) + B_d(KS(k) + Z(k))], \\ \hat{D}(k) = KS(k) + Z(k) \end{cases} \tag{21}$$

where $Z(k)$ is the internal state vector of the observer, and $K \in \mathbb{R}^{2\times 2}$ is the diagonal matrix to be designed.

Define the estimation error $E_d(k) = D(k) - \hat{D}(k) = [e_1(k), e_2(k)]^{\mathrm{T}}$, then the error dynamics for (21) is described as

$$\begin{aligned} E_d(k+1) &= D(k+1) - \hat{D}(k+1) \\ &= D(k+1) - K[AS(k) + B_u U(k) + B_d D(k)] \\ &\quad - Z(k) + K[B_u U(k) + B_d \hat{D}(k)] \\ &= D(k+1) - KB_d E_d(k) + K(I_{2\times 2} - A)S(k) - \hat{D}(k) \\ &= (I_{2\times 2} - KB_d)E_d(k) + \Delta D(k+1) \end{aligned} \tag{22}$$

where $\Delta D(k+1) = D(k+1) - D(k)$.

Lemma 1. *With the design of observer (21), it is always possible to estimate the disturbance $D(k)$ within a bounded estimation error if the matrix K is chosen as $(I_{2\times 2} - \Lambda)B_d^{-1}$ where $\Lambda = \mathrm{diag}\{\lambda_1, \lambda_2\}$ with $|\lambda_i| < 1, i = 1, 2$.*

Substituting $K = (I_{2\times 2} - \Lambda)B_d^{-1}$ into (22) results in error dynamics as

$$e_i(k+1) = \lambda_i e_i(k) + \Delta d_i(k+1), \ i = 1, 2. \tag{23}$$

Solving (23) by using the iterative operation, we have

$$e_i(k) = \lambda_i^k e_i(0) + \sum_{j=1}^{k} \lambda_i^{k-j} \Delta d_i(j), \ i = 1, 2. \tag{24}$$

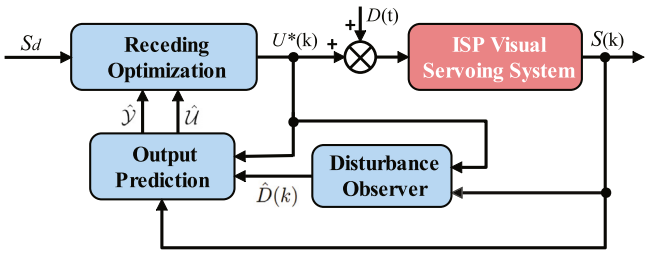

Fig. 2. Implementation diagram of the proposed method.

Under Assumption 2, the steady-state errors of observer (21) can be further estimated by

$$\begin{aligned} \lim_{k\to\infty} |e_i(k)| &\le \lim_{k\to\infty} \left(\sum_{j=1}^{k} |\lambda_i|^{k-j} |\Delta d_i(j)| \right) \\ &\le \lim_{k\to\infty} \frac{(1 - |\lambda_i|^k)T_s\varepsilon_i}{1 - |\lambda_i|} = \frac{T_s\varepsilon_i}{1 - |\lambda_i|}, \ i = 1, 2. \end{aligned} \tag{25}$$

This completes the proof.

The implementation diagram of the proposed approach is depicted in Fig. 2.

3.5. Stability analysis

Define the output tracking error $E_s(k) = S(k) - S_d$. By substituting (17) into system (8), the dynamics of the output tracking error is given by

$$\begin{aligned} E_s(k+1) = (A - B_u K_m)E_s(k) + B_d E_d(k) \\ + (A - B_u K_m + B_u K_s - I_{2\times 2})S_d. \end{aligned} \tag{26}$$

Moreover, one has $\mathcal{I}_S = F$ and $K_m = K_s$ due to $A = I_{2\times 2}$. Therefore, Eq. (26) reduces to

$$E_s(k+1) = (A - B_u K_m)E_s(k) + B_d E_d(k). \tag{27}$$

Combining (27) with observer error dynamics (22), the extended closed-loop error system is governed by

$$\mathcal{E}(k+1) = \mathcal{A}\mathcal{E}(k) + \mathcal{G}(k) \tag{28}$$

where

$$\mathcal{E}(k) = \begin{bmatrix} E_d(k) \\ E_s(k) \end{bmatrix}, \mathcal{G}(k) = \begin{bmatrix} \Delta D(k+1) \\ O_{2\times 1} \end{bmatrix},$$
$$\mathcal{A} = \begin{bmatrix} I_{2\times 2} - KB_d & O_{2\times 2} \\ B_d & I_{2\times 2} - B_u K_m \end{bmatrix}.$$

The stability is analyzed by the following theorem.

Lemma 2. *Let $\|\bullet\|$ be a norm on matrix[$\bullet$]. For any given non-zero matrices $A \in \mathbb{R}^{n\times n}, x \in \mathbb{R}^n$, if the spectral radius of A satisfies $\rho(A) < 1$, there always exists a positive constant $r \in [\rho(A), 1)$ such that $\|A^k x\| \le r^k \|x\|, k \in \mathbb{R}^+$.*

Letting λ be any eigenvalue of A, one has $Ax = \lambda x$, then $\|Ax\| \le \rho(A)\|x\| \le r\|x\|$. Furthermore, through the iterative operations,

$$\|A^k x\| \le r\|A^{k-1}x\| \le \cdots \le r^k \|x\|.$$

The proof is completed.

Theorem 1. *Suppose that Assumptions 1–2 hold for system (8). By assigning proper values for the observer gain matrix K and weighting matrices $\bar{\mathcal{Q}}$ as well as $\bar{\mathcal{R}}$, such that all eigenvalues of matrices $(I_{2\times 2} - KB_d)$ and $(I_{2\times 2} - B_u K_m)$ are located inside the unit circle, the output tracking error asymptotically converges to a bounded region with proposed optimized control law (19).*

Table 1
Nominal Intrinsic Parameters of the Camera.

Meaning	Parameter	Unit	Value
Scaling factor of x axis	k_x^*	pixel/m	178571
Scaling factor of y axis	k_y^*	pixel/m	178571
Principal point coordinate of x axis	u_0	pixel	320
Principal point coordinate of y axis	v_0	pixel	240
Focal length	λ^*	mm	16

It is explicit that the characteristic equation of matrix $\mathcal{A}$ is determined by

$$\begin{aligned}\det(\lambda I_{4\times4} - \mathcal{A}) = \det(\lambda I_{2\times2} - (I_{2\times2} - KB_d)) \\ \times \det(\lambda I_{2\times2} - (I_{2\times2} - B_u K_m)) = 0.\end{aligned} \tag{29}$$

From (29), we can obtain that all the eigenvalues of $\mathcal{A}$ are located inside the unit circle, i.e., $|\lambda_i(\mathcal{A})| < 1, (i = 1, \cdots, 4)$.

Furthermore, solving closed-loop system (28) yields

$$\mathcal{E}(k) = \mathcal{A}^k \mathcal{E}(0) + \sum_{j=0}^{k-1} \mathcal{A}^{k-j-1} \mathcal{G}(j). \tag{30}$$

According to Lemma 2, $\mathcal{E}(k)$ satisfies

$$\begin{aligned}\|\mathcal{E}(k)\| &\le \|\mathcal{A}^k \mathcal{E}(0)\| + \sum_{j=0}^{k-1} \|\mathcal{A}^{k-j-1} \mathcal{G}(j)\| \\ &\le r^k \|\mathcal{E}(0)\| + \sum_{j=0}^{k-1} r^{k-j-1} \|\mathcal{G}(j)\|.\end{aligned} \tag{31}$$

Under Assumption 2, we have $\|\mathcal{G}(j)\| \le T_s\sqrt{\varepsilon_1^2 + \varepsilon_2^2}$. Then, the ultimate tracking error of closed-loop system (28) can be estimated by

$$\begin{aligned}\lim_{k\to\infty} \|\mathcal{E}(k)\| &\le T_s\sqrt{\varepsilon_1^2 + \varepsilon_2^2} \lim_{k\to\infty} \sum_{j=0}^{k-1} r^{k-j-1} \\ &= \frac{T_s}{1-r}\sqrt{\varepsilon_1^2 + \varepsilon_2^2}\end{aligned} \tag{32}$$

which completes the proof.

4. Experimental results

4.1. Experimental setup

To verify mentioned advantages of the proposed approach, the experiments are organized in this section. The experimental setups of an ISP visual servoing system and a simulated moving target are shown in Fig. 3. The ISP system comprises the camera (DFK21BU04), the pitch-yaw gimbals, the embedded controller (DSP2812), the simulated carrier, and the image processing software. The nominal parameters of the camera are shown in Table 1. Moreover, the position information of the target in the image plane is transmitted by the image processing unit at intervals of 100 ms, i.e., $T_s = 100$ ms. Meanwhile, to measure the inertial angular velocities of the camera for the inner-loop controller, a two-axes fiber optical gyroscope (FOG) is fixed on the inner gimbal.

Remark 4. Since the linear controller is designed for the inner loop, a rapid-changing given angular velocity will most likely cause the input saturation problem. Fortunately, this situation is almost not easy to happen in this system with the following two reasons. Firstly, the tracking ability of the inner loop fully meets the requirements of the visual servoing loop, because the moving speed of the target in the image plane is relatively slow. Secondly, the control period of the inner loop is only 1 ms, which is much faster than that of the outer loop, so that the inner-loop controller has enough time to reach the desired angular velocity with appropriate gains, which makes the intense dynamic response of the inner loop avoided.

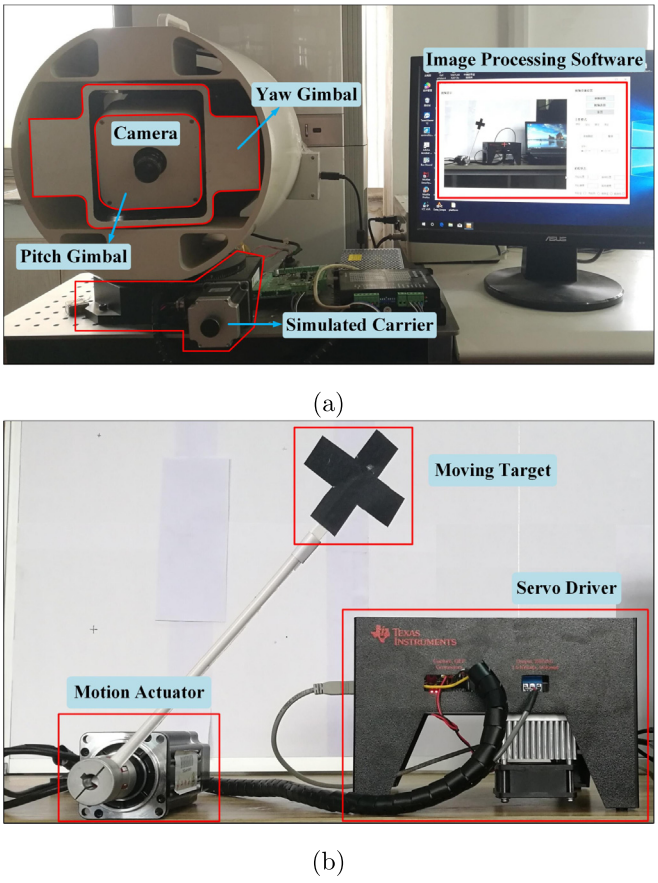

Fig. 3. Experimental setups: (a) Two-axes ISP visual servoing system and (b) Simulated moving target.

4.2. Parameters selection

The parameters selection has crucial influences on the control performance of the closed-loop system. To this end, we will conduct detailed discussions on the parameters selection of the proposed control approach in this subsection. The parameters of the benchmark being compared are set as $N_p = 25$, $N_c = 5$, $\bar{\mathcal{Q}} = I_{2\times2}$, $\bar{\mathcal{R}} = 0.35I_{2\times2}$, and $K = \text{diag}(6.5, 6.5)$. In this test, the target is stationary and the initial position of the target is located at the coordinate $[+140, +145]$ relative to the principal point in the image plane.

4.2.1. Horizon length

In order to quantitatively describe the dynamic response of the system, the reaching time is selected as the performance index. It can be found that the dynamics is greatly impacted by assignments of the prediction horizon N_p and the control horizon N_c from Figs. 4 and 5. The x-axis controllers with N_p set to 30, 25, and 20 result in reaching times of 0.8 s, 1.1 s, and 1.5 s, respectively. It shows that a larger N_p causes a faster convergence rate but may lead to an unsatisfactory overshoot of the system output. For a fixed control horizon N_c, increasing N_p means that more errors between predicted outputs and references need to

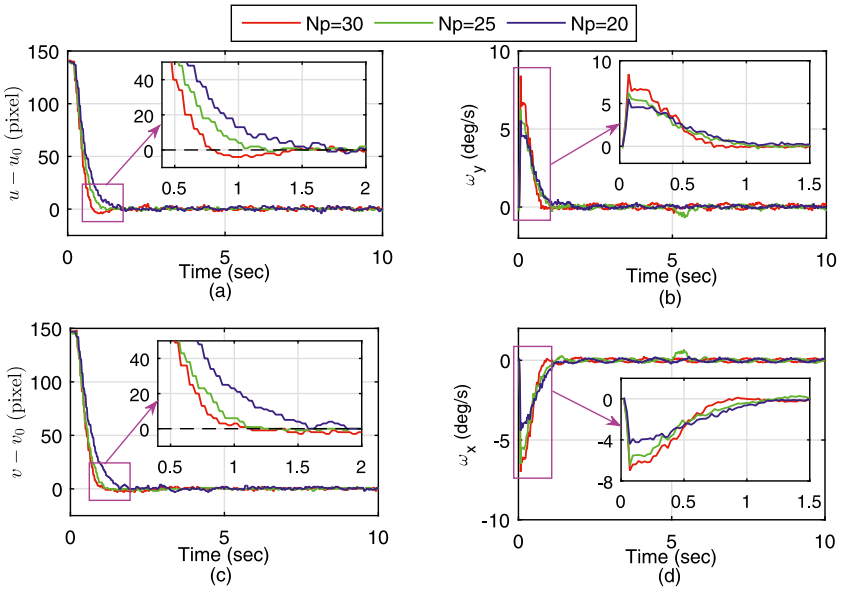

Fig. 4. Tracking performances with different prediction horizons N_p: (a) x-axis positions, (b) y-axis angular velocities, (c) y-axis positions, and (d) x-axis angular velocities.

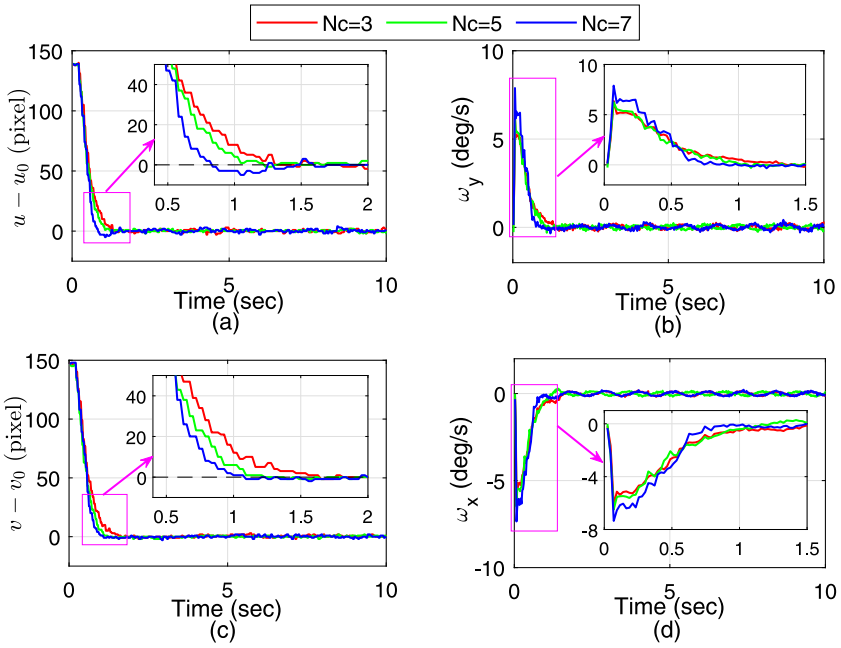

Fig. 5. Tracking performances with different control horizons N_c: (a) x-axis positions, (b) y-axis angular velocities, (c) y-axis positions, and (d) x-axis angular velocities.

be cumulated in cost function (12). Therefore, it is necessary to reduce the errors by generating aggressive control inputs so that the cost function J is minimized. We can also find that the x-axis controllers with N_c of 3, 5, and 7 produce reaching times of 1.4 s, 1.0 s, and 0.8 s, respectively. The response of the system becomes faster with a larger N_c, because the proposed approach produces larger gains K_s and K_m when the control horizon N_c is increased. Similarly, the y-axis responses also indicate the above conclusions. Furthermore, it should be pointed out that an addition in N_c will inevitably aggravate the computational burden of the receding optimization due to the extension of dimensions of Φ_u and Φ_d in (11).

4.2.2. Weighting matrix

The weighting matrices $\bar{\mathcal{Q}}$ and $\bar{\mathcal{R}}$ in cost function (12) are used to penalize the tracking error and the control energy. In general, increasing $\bar{\mathcal{Q}}$ will speed up the convergence rate of the tracking error while increasing $\bar{\mathcal{R}}$ will restrict the control energy. For a fixed $\bar{\mathcal{R}}$, adding $\bar{\mathcal{Q}}$ means that the error correlation term has a larger proportion in the cost function, therefore the proposed algorithm expands the control input to make the output error smaller to obtain a smaller J. On the contrary, a relatively larger $\bar{\mathcal{R}}$ matrix makes the control input correlation term has higher weight, so that the optimization method produces a smaller control input to ensure the minimization of the cost function.

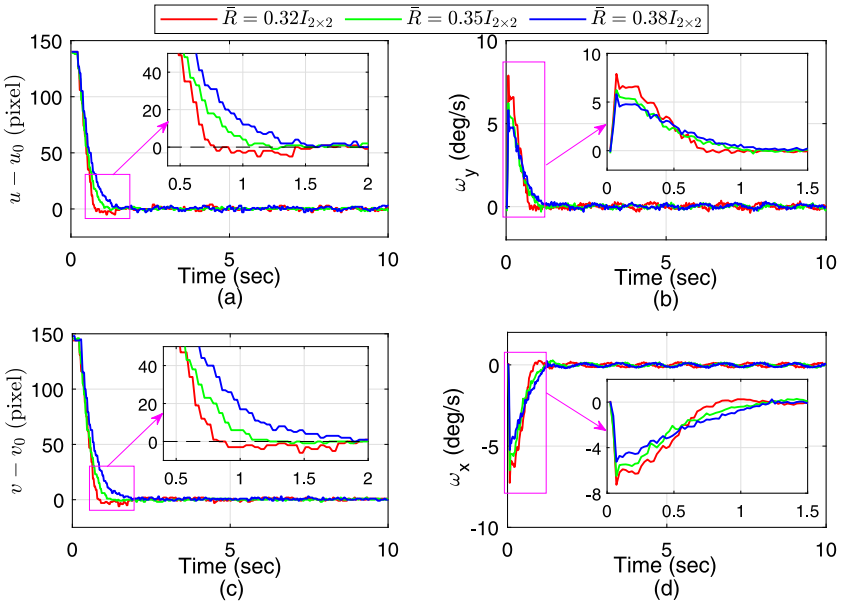

Fig. 6. Tracking performances with different weighting matrices $\bar{\mathcal{R}}$: (a) x-axis positions, (b) y-axis angular velocities, (c) y-axis positions, and (d) x-axis angular velocities.

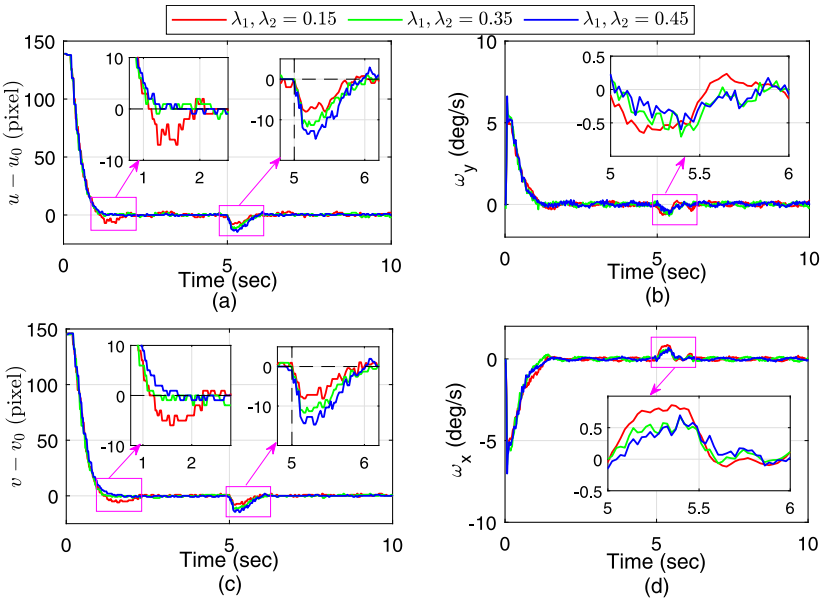

Fig. 7. Tracking performances with different observer gains K: (a) x-axis positions, (b) y-axis angular velocities, (c) y-axis positions, and (d) x-axis angular velocities.

In practice, we primarily choose the identity matrix $I_{2\times2}$ as the $\bar{\mathcal{Q}}$, and then adjust the other one for better control performances. As depicted in Fig. 6, a smaller $\bar{\mathcal{R}}$ results in faster convergence rate, but may increase the control energy and cause a poor dynamic of the system output.

4.2.3. Observer gain

As suggested in Lemma 1, the disturbance observer gain K can be used to adjust the ultimate bound of the disturbance estimation error. Theoretically, when (λ_1, λ_2) is close to $(0, 0)$, i.e., K is close to $\text{diag}(1/T_s, 1/T_s)$, the estimation error can be regulated relatively small, which results in a much shorter recovery time for the output after the disturbance exists. To verify this statement, the experimental test where the target moves rapidly toward a new position at 5 s is performed. As depicted in Fig. 7, stronger robustness against the disturbance is obtained by selecting a smaller gain (λ_1, λ_2). However, note that the too small value leads to increases of measurement noises and output fluctuations.

From the above analysis, it is obtained that the tradeoffs among dynamic performance, steady-state accuracy, and computational burden should be taken into consideration by choosing appropriate horizon lengths, weighting matrices, and the disturbance observer gain.

4.3. Performance comparison

Control approaches of the traditional PID control, the integrator-based MPC (I-MPC) in [27], and the error-based feedforward control (EBF) in [34] are employed for the purpose of performance comparisons. To ensure the fairness, the principle of setting parameters of these controllers is to make their curves of step responses basically coincide. The proportional and integral

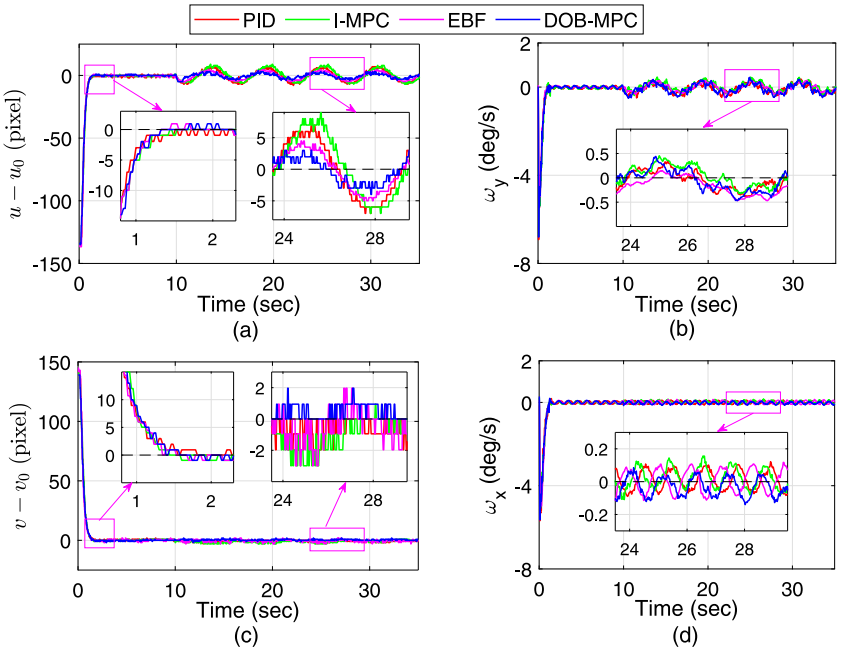

Fig. 8. Tracking performances in the presence of carrier motion: (a) *x*-axis positions, (b) *y*-axis angular velocities, (c) *y*-axis positions, and (d) *x*-axis angular velocities.

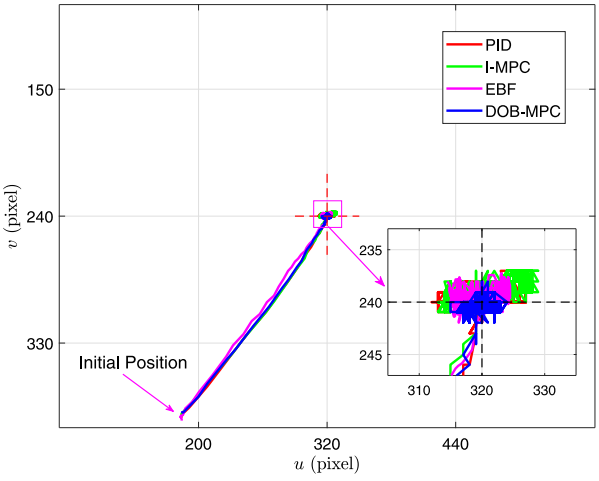

Fig. 9. Feature trajectories of the target in the image plane in Case I.

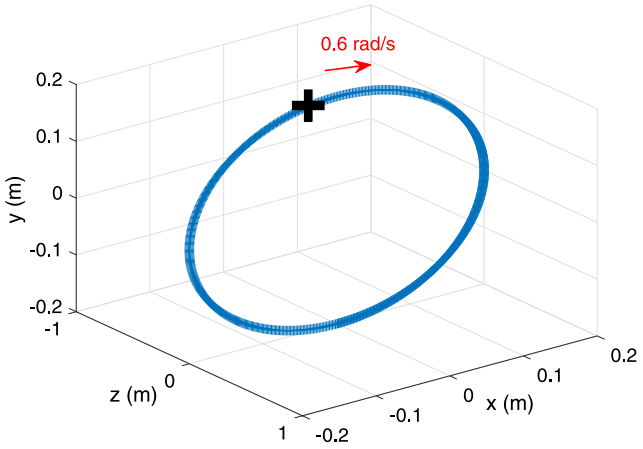

Fig. 10. Target trajectory in 3D space.

gains of the PID controller for both *x* and *y* axes are set as 0.02 and 0.005, respectively. The tuning parameter τ in the Q-filter of the EBF controller is set as 1.5, and the proportional and integral gains of the base feedback control law are 0.015 and 0.002. The predictive horizon, the control horizon, and weighting matrices of the I-MPC method and the DOB-MPC approach are both set as $N_p = 25$, $N_c = 5$, and $\mathcal{R} = 0.35\mathcal{Q} = 0.35I_{2\times2}$, respectively. Moreover, the gain matrix of the DOB is chosen as $K = \text{diag}(6.5, 6.5)$.

In order to quantitatively analyze the tracking error and the control effect of each method, variables of the offset, the maximum absolute (MA), the root-mean-squared (RMS), and the total variation (TV) are selected as performance indicators. The calculation of each indicator is as follows. The offset is defined as the absolute of the mean of tracking errors in steady state, the MA means the maximum of absolutes of a series of data, the RMS denotes the square root of the average of squares of a set of numbers, and the TV is defined as the sum of the absolute values of changes of control efforts.

4.3.1. Case I-Tracking performance in the presence of carrier motion

The movement of the carrier results in the inner-loop tracking error, reducing the control performance of the system. Therefore, the suppression abilities of four methods to the carrier disturbance are verified firstly. In the test, both of target and carrier are stationary at the beginning and the initial position of target is set at the coordinate of $[-140, +145]$ relative to the principal point in the image plane. After 10 s, the carrier starts to run a sinusoidal motion with the period of 6 s and the amplitude of 50 *deg*. Since the target is immobile, the effects of the unknown feature depth coupled with the target motion can be negligible. The experimental results of this case are shown in Figs. 8 and 9.

As shown in Fig. 8, four methods produce similar step responses at the beginning, indicating that the selection of control parameters is relatively fair. When the carrier starts to move at 10 s, the proposed DOB-MPC approach shows the stronger robustness against the uncertainties. Compared with the other methods, the proposed approach reduces the offset by 14% to 36% from Table 2. As far as the RMS index is concerned, the

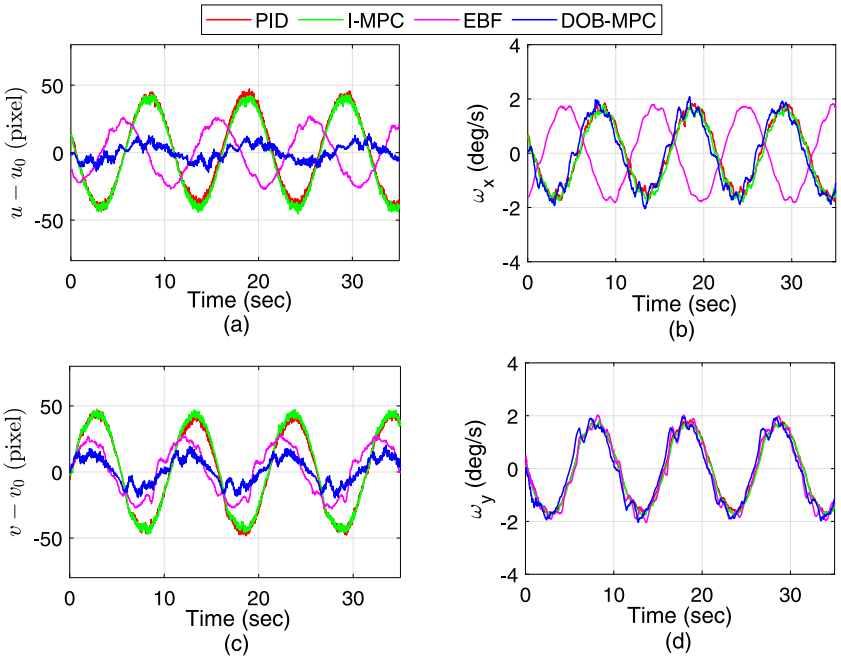

Fig. 11. Tracking performances in the presence of target motion: (a) *x*-axis positions, (b) *y*-axis angular velocities, (c) *y*-axis positions, and (d) *x*-axis angular velocities.

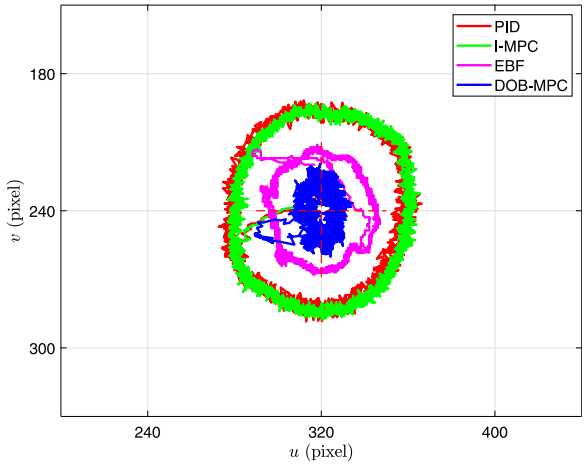

Fig. 12. Feature trajectories of the target in the image plane in Case II.

tracking accuracy of the DOB-MPC is twice as high as the PID and the I-MPC, and more than 13% higher than that of the EBF. It should be noted that there is no significant difference in the control actions of the four methods. The feature trajectories of four control methods in the image plane are shown in Fig. 9.

4.3.2. Case II-Tracking performance in the presence of target motion

In this case, the target moves circularly at the speed of 0.6 rad/s, and the radius is 275 pixels in the image plane, as shown in Fig. 10. The unknown time-varying feature depth coupled with the target motion restricts the visual servoing performance. The experimental results of target tracking errors are presented in Figs. 11 and 12.

Although the TV values of control inputs of comparison methods are at the similar level, the RMS values of tracking errors produced by the DOB-MPC are only 5.82 and 9.55 pixels in *x* and *y* axes, less than 1/3 of those by the PID as well as the I-MPC, and 3/4 by the EBF.

Table 2
Performance Indexes With Four Control Schemes.

Control schemes		*x* axis				*y* axis			
		Offset	MA	RMS	TV	Offset	MA	RMS	TV
Case I	PID	0.42	8.50	4.58	582	0.47	2.17	1.32	574
	I-MPC	0.48	8.19	4.51	612	0.49	2.14	1.29	626
	EBF	0.52	4.94	2.23	574	0.44	2.09	0.82	598
	DOB-MPC	0.36	4.01	1.94	565	0.31	1.96	0.68	607
Case II	PID	1.57	47.28	28.52	414	2.04	48.38	33.25	462
	I-MPC	1.76	45.39	30.26	409	1.85	49.16	31.49	470
	EBF	0.43	22.58	10.76	402	0.76	24.88	12.97	458
	DOB-MPC	0.29	14.15	5.82	405	0.17	19.67	9.55	452
Case III	PID	1.44	62.34	37.22	428	2.34	55.87	34.25	479
	I-MPC	1.36	61.19	36.15	420	2.06	54.92	32.76	482
	EBF	0.56	27.37	14.82	407	0.81	32.98	16.45	467
	DOB-MPC	0.32	21.24	10.34	411	0.21	24.38	13.21	458

Thanks to the active disturbance estimation and compensation, the proposed control method shows the strong robustness against time-varying uncertainties, whereas it can only ensures relatively large tracking errors by taking the integral manner for PID and I-MPC approaches. Besides, coupled kinematic model (7) is clearly established and the predictive control is employed as the base control law, while the ignored coupling terms in the EBF approach are considerable when the speed of the target is large.

4.3.3. Case III-Tracking performance with both target and carrier motions

In this case, motions of the target and the carrier are both considered. The movement of the target is the same as the previous case with the time-varying feature depth, and the carrier is with a sinusoidal motion of 1.1 rad/s. The experimental results are shown in Fig. 13.

For the MA of the output errors, the proposed method has a 55% to 65% mitigation relative to the PID and the I-MPC, and at least 22% lower than the EBF. With similar control energies, the RMS of tracking errors is decreased by 19% to 72% compared with the other controllers. Furthermore, the specific performances of four methods in three cases are summarized in Table 2.

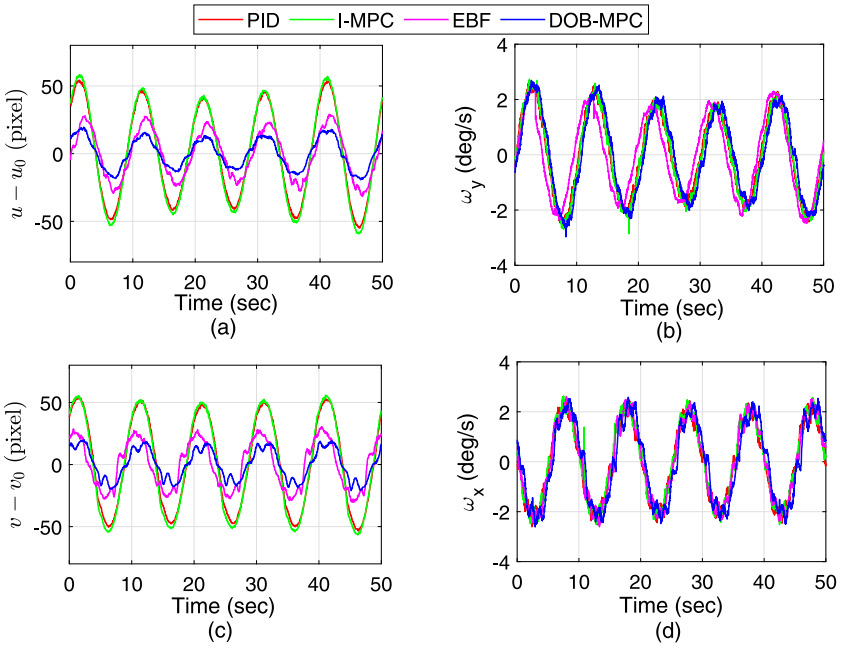

Fig. 13. Tracking performances in the presence of both target and carrier motions: (a) *x*-axis positions, (b) *y*-axis angular velocities, (c) *y*-axis positions, and (d) *x*-axis angular velocities.

5. Conclusion

In this paper, an IBVS method based on the DOB-MPC has been proposed for the tracking loop of the ISP system. First, a depth-independent kinematic matrix has been obtained by employing the partitioned approach in the system modeling. The uncertain kinematics arising from the unknown feature depth, inner-loop angular rate tracking errors, and uncalibrated intrinsic parameters has been treated as the lumped uncertainties and estimated in real time by the designed discrete-time DOB. To suppress effects of the uncertainty, the disturbance estimate has been actively incorporated into the receding optimization process. It has been proved that the output error asymptotically converges to a bounded region, which can be quantitatively adjusted. Experimental studies have been carried out to show the effectiveness of the proposed method.

Besides, we did not pay too much attention to output and input constraints in theoretical analysis and experiments because they are not major problems in this system. The limited outputs of *x* and *y* axes are 320 and 240 pixels, ensuring the system has sufficient space in nominal operation. And the largest tracking angular velocity of the inner loop is 50 deg/s, which is much faster than the given one by the outer loop. However, variable constraints exist in many practical applications, such as the high-speed manipulator. Fortunately, the MPC is a technique that has advantage to handle system various constraints. Therefore, the design of the constrained MPC combined with the disturbance compensation will be one of the focuses of our future researches.

Declaration of competing interest

The authors declare that they have no known competing financial interests or personal relationships that could have appeared to influence the work reported in this paper.

Acknowledgments

This work is supported in part by the National Natural Science Foundation of China under Grant 61973080, Grant 61973081, Grant 61633003, and Grant 62025302.

References

[1] He Q, Zeng C, Gao Z. Analysis and design of the stewart platform-based parallel support bumper for inertially stabilized platforms. IEEE Trans Ind Electron 2020;67(5):4203–15.
[2] Königseder F, Kemmetmüller W, Kugi A. Attitude control strategy for a camera stabilization platform. Mechatronics 2017;46:60–9.
[3] Zhou X, Gao H, Zhao B, Zhao L. A GA-based parameters tuning method for an ADRC controller of ISP for aerial remote sensing applications. ISA Trans 2018;81:318–28.
[4] Lin Z, Liu K, Zhang W. Inertially stabilized platform for airborne remote sensing using magnetic bearings. IEEE/ASME Trans Mechatronics 2016;21(1):288–301.
[5] Zhou X, Zhao B, Liu W, Yue H, Yu R, Zhao Y. A compound scheme on parameters identification and adaptive compensation of nonlinear friction disturbance for the aerial inertially stabilized platform. ISA Trans 2017;67:293–305.
[6] Hurák Z, Řezáč M. Image-based pointing and tracking for inertially stabilized airborne camera platform. IEEE Trans Control Syst Technol 2012;20(5):1146–59.
[7] Pan S, Wu Y, Zhang J, Zhou S, Zhu H. Modeling and control of a 2-degree-of-freedom gyro-stabilized platform driven by ultrasonic motors. J Intell Mater Syst Struct 2018;29(11):2324–32.
[8] Safa A, Abdolmalaki RY. Robust output feedback tracking control for inertially stabilized platforms with matched and unmatched uncertainties. IEEE Trans Control Syst Technol 2019;27(1):118–31.
[9] Ke D, Cong S, Kong D, Shen H. Discrete-time direct model reference adaptive control application in a high-precision inertially stabilized platform. IEEE Trans Ind Electron 2019;66(1):358–67.
[10] Mao J, Yang J, Liu X, Li S, Li Q. Modeling and robust continuous TSM control for an inertially stabilized platform with couplings. IEEE Trans Control Syst Technol 2020;28(6):2548–55.
[11] Zhang K, Chen J, Li Y. Unified visual servoing tracking and regulation of wheeled mobile robots with an uncalibrated camera. IEEE/ASME Trans Mechatronics 2018;23(4):1728–39.
[12] Li B, Zhang X, Fang Y. Visual servoing of wheeled mobile robots without desired images. IEEE Trans Cybern 2019;49(8):2835–44.
[13] Song X, Fu M. CLFs-based optimization control for a class of constrained visual servoing systems. ISA Trans 2017;67:507–14.
[14] Li T, Zhao H. Global finite-time adaptive control for uncalibrated robot manipulator based on visual servoing. ISA Trans 2017;68:402–11.
[15] Serra P, Cunha R, Hamel T, Cabecinhas D, Silvestre C. Landing of a quadrotor on a moving target using dynamic image-based visual servo control. IEEE Trans Robot 2016;32(6):1524–35.
[16] Asl HJ, Yoon J. Adaptive vision-based control of an unmanned aerial vehicle without linear velocity measurements. ISA Trans 2016;65:296–306.
[17] Chaumette F, Hutchinson S. Visual servo control. I. Basic approaches. IEEE Robot Autom Mag 2006;13(4):82–90.

[18] Janabi-Sharifi F, Deng L, Wilson WJ. Comparison of basic visual servoing methods. IEEE/ASME Trans Mechatronics 2011;16(5):967–83.
[19] Spong MW, Hutchinson S, Vidyasagar M. Robot modeling and control. New York: Wiley; 2006.
[20] Shi H, Sun G, Wang Y, Hwang K-S. Adaptive image-based visual servoing with temporary loss of the visual signal. IEEE Trans Ind Electron 2019;15(4):1956–65.
[21] Mao J, Li S, Li Q, Yang J. Design and implementation of continuous finite-time sliding mode control for 2-DOF inertially stabilized platform subject to multiple disturbances. ISA Trans 2019;84:214–24.
[22] Shirzadeh M, Amirkhani A, Jalali A, Mosavi MR. An indirect adaptive neural control of a visual-based quadrotor robot for pursuing a moving target. ISA Trans 2015;59:290–302.
[23] Zheng D, Wang H, Wang J, Chen S, Chen W, Liang X. Image-based visual servoing of a quadrotor using virtual camera approach. IEEE/ASME Trans Mechatronics 2017;22(2):972–82.
[24] Bourquardez O, Mahony R, Guenard N, Chaumette F, Hamel T, Eck L. Image-based visual servo control of the translation kinematics of a quadrotor aerial vehicle. IEEE Trans Robot 2009;25(3):743–9.
[25] Mayne DQ. Model predictive control: recent developments and future promise. Automatica 2014;50(12):2967–86.
[26] Wang Y, Hou M. Model-free adaptive integral terminal sliding mode predictive control for a class of discrete-time nonlinear systems. ISA Trans 2019;93:209–17.
[27] Wang L. Model predictive control system design and implementation using MATLAB. London: Springer-Verlag; 2009.
[28] Kim KS, Rew KH. Reduced order disturbance observer for discrete-time linear systems. Automatica 2013;49(4):968–75.
[29] Chen W-H, Yang J, Guo L, Li S. Disturbance-observer-based control and related methods–An overview. IEEE Trans Ind Electron 2016;63(2):1083–95.
[30] Yang J, Zheng W, Li S, Wu B, Cheng M. Design of a prediction-accuracy-enhanced continuous-time MPC for disturbed systems via a disturbance observer. IEEE Trans Ind Electron 2015;62(9):5807–16.
[31] Byrnes CI, Priscoli FD, Isidori A. Output regulation of uncertain nonlinear systems. Boston: Birkhauser; 1997.
[32] Xue W, Huang Y. On performance analysis of ADRC for a class of MIMO lower-triangular nonlinear uncertain systems. ISA Trans 2014;53:955–62.
[33] Cai W, She J, Wu M, Ohyama Y. Disturbance suppression for quadrotor UAV using sliding-mode-observer-based equivalent-input-disturbance approach. ISA Trans 2019;92:286–97.
[34] Tang T, Yang T, Qi B, Ren G, Bao Q. Error-based feedforward control for a charge-coupled device tracking system. IEEE Trans Ind Electron 2019;66(10):8172–80.